

Influence of ultra-low ethylene partial pressure on microstructural and compositional evolution of sputter-deposited Zr-C thin films

Hicham Zaid, Angel Aleman, Koichi Tanaka, Chao Li, Pascal Berger, Tyson Back, Joshua Fankhauser, Mark S. Goorsky, Suneel Kodambaka

▶ **To cite this version:**

Hicham Zaid, Angel Aleman, Koichi Tanaka, Chao Li, Pascal Berger, et al.. Influence of ultra-low ethylene partial pressure on microstructural and compositional evolution of sputter-deposited Zr-C thin films. Surface and Coatings Technology, 2020, 398, pp.126053. 10.1016/j.surfcoat.2020.126053 . cea-02884587

HAL Id: cea-02884587

https://cea.hal.science/cea-02884587

Submitted on 30 Jun 2020

HAL is a multi-disciplinary open access archive for the deposit and dissemination of scientific research documents, whether they are published or not. The documents may come from teaching and research institutions in France or abroad, or from public or private research centers.

L'archive ouverte pluridisciplinaire **HAL**, est destinée au dépôt et à la diffusion de documents scientifiques de niveau recherche, publiés ou non, émanant des établissements d'enseignement et de recherche français ou étrangers, des laboratoires publics ou privés.

Influence of ultra-low ethylene partial pressure on microstructural and compositional evolution of sputter-deposited Zr-C thin films

Hicham Zaid[a,*], Angel Aleman[b], Koichi Tanaka[a], Chao Li[a], Pascal Berger[c], Tyson Back[d], Josh Fankhauser[a], Mark S. Goorsky[a], and Suneel Kodambaka[a]

[a] Department of Materials Science and Engineering, University of California Los Angeles, 410 Westwood Plaza, Los Angeles, CA 90095 USA
[b] Department of Mechanical and Aerospace Engineering, University of California Los Angeles, 420 Westwood Plaza, Los Angeles, CA 90095 USA
[c] Université Paris-Saclay, CEA, CNRS, NIMBE, 91191, Gif-sur-Yvette, France
[d] Air Force Research Laboratory, Wright Patterson AFB, OH 45433-7707

*email: hizaid@ucla.edu

Abstract

Zr-C thin films are grown on single-crystalline MgO(001) substrates via ultra-high vacuum dc magnetron sputtering of Zr target in 10 mTorr Ar-C_2H_4 gas mixtures with ethylene partial pressures ($p_{C_2H_4}$) between 2×10^{-7} Torr and 2×10^{-4} Torr at substrate temperature T_s = 923 K and using $p_{C_2H_4} = 2 \times 10^{-6}$ Torr at 723 K $\leq T_s \leq$ 1123 K. The as-deposited layer microstructure and composition are determined using X-ray diffraction, transmission electron microscopy, and X-ray photoelectron spectroscopy. We find that the layers sputter-deposited at T_s = 923 K using the lowest $p_{C_2H_4} = 2 \times 10^{-7}$ Torr are polycrystalline, close-packed hexagonal structured Zr:C solid solutions. At higher $p_{C_2H_4} = 2 \times 10^{-6}$ Torr and 2×10^{-5} Torr, we obtain films composed of free-carbon (C) and NaCl-structured ZrC_x, $x \leq 1$. The amount of C increases 104% with ten-fold increase in $p_{C_2H_4}$ from 2×10^{-6} Torr to 2×10^{-5} Torr. At the highest $p_{C_2H_4} = 2 \times 10^{-4}$ Torr, the layers are X-ray amorphous with ~ 49 at.% C. Films grown at 723 K $\leq T_s \leq$ 1123 K using constant $p_{C_2H_4} = 2 \times 10^{-6}$ Torr exhibit qualitatively similar microstructures, irrespective of T_s, composed of dense columnar ZrC_x grains surrounded by C and corrugated surfaces. Our results suggest that the compositional and microstructural evolution of Zr-C films during reactive

sputter-deposition of Zr is highly sensitive to ethylene partial pressure, with as little as 0.02% of the total pressure sufficient at $T_s \geq 723$ K to obtain ZrC_x films.

Keywords: transition-metal carbides, reactive magnetron sputtering, Zr-C thin films

1. Introduction

Group 4 to 6 transition-metal carbides (TMCs) are highly refractory compounds with excellent thermomechanical and thermochemical properties due to a mixture of ionic, covalent, and metallic bonds between the metal cations and carbon anions. Among the TMCs, ZrC crystallizes in B1 (rock salt) structure ($Fm\bar{3}m$; space group 225) with a bulk lattice parameter a_o = 0.4693 nm at room temperature [1]. ZrC is a hard (> 25 GPa), high elastic modulus (> 350 GPa), and high melting point (> 3673 K) solid with good thermal (20.5 W/m.K at 293 K) and electrical conductivities (2326 S/m at 293 K) and excellent resistance to wear, corrosion, and oxidation [2]. ZrC is used as hard protective coatings on cutting tools [3–7], as structural components in aerospace vehicles, as coating material for nuclear fuel in nuclear reactors [2,3,8–11], and as field-emission cathodes in electronic devices [12].

ZrC thin films have been grown via reactive sputtering of elemental Zr in hydrocarbon/Ar gas mixtures [3,13], sputtering of compound ZrC [14,15] and Zr and C targets [16] in pure Ar discharges, sol-gel synthesis [17], chemical vapor deposition [18–20], and pulsed laser deposition [21,22]. Among all these techniques, reactive sputter-deposition has been the most commonly used method to grow ZrC and other TMC thin films [3,13,16,23–28]. In this approach, one can control both the thin film composition and the growth rate by appropriate choice of the reactive gas and its flux [29]. The TMC coatings deposited via this technique typically result in two-phase mixtures, composed of TMC crystallites and free-carbon (C) [3,24,27], with reactive gas pressure-dependent TMC and C phase fractions, crystallinity, and mechanical properties [3,24,26,27,30]. Recently, Tanaka *et al*. [31] have demonstrated tunability of Ta-C phase composition in thin films sputter-deposited with ultra-low amounts of ethylene partial pressures, $p_{C_2H_4}$ (0.0025 ~ 2.5% of total pressure) using a compound TaC target. Here, we focus on the

microstructural and compositional evolutions of thin films deposited by sputtering elemental Zr target using similarly low $p_{C_2H_4}$ between 0.002 and 2% of the total pressure.

In this paper, we report on the effects of $p_{C_2H_4}$ (between 2×10^{-7} Torr and 2×10^{-4} Torr) and substrate temperature ($723\ K \leq T_s \leq 1123\ K$) on the composition and crystallinity of Zr-C/MgO(001) thin films sputter-deposited in 10 mTorr Ar-C_2H_4 gas mixtures. (Here, and in the following sections, we use Zr-C to refer to both Zr:C solid solutions and ZrC_x, $x \leq 1$, compounds.) Using X-ray diffraction (XRD), transmission electron microscopy (TEM), and X-ray photoelectron spectroscopy (XPS), we characterized the as-deposited layer microstructure and composition. We find that the films sputter-deposited at $T_s = 923$ K using $p_{C_2H_4} = 2 \times 10^{-7}$ Torr are polycrystalline with primarily hexagonal close-packed (hcp) Zr:C solid solutions. At $p_{C_2H_4} = 2 \times 10^{-6}$ Torr and 2×10^{-5} Torr, the films are composed of a two-phase mixture of B1-structured ZrC_x and C with an increasing phase fraction of C with increasing $p_{C_2H_4}$. At $p_{C_2H_4} = 2 \times 10^{-4}$ Torr, the film is X-ray amorphous and with a high C content. The Zr-C layers sputter-deposited with $p_{C_2H_4} = 2 \times 10^{-6}$ Torr at T_s between 723 K and 1123 K are all two-phase mixtures of B1-ZrC_x and C with little changes in the C content with increasing T_s. Our experiments reveal that the carbon content in reactively sputter-deposited Zr-C thin films is highly sensitive to the reactive gas pressure.

2. Experimental details

All the Zr-C films are grown on single-side polished $0.5 \times 2 \times 10$ mm^3 rectangular strips of MgO(001) substrates in a custom-designed ultra-high vacuum (UHV, base pressure < 5.3×10^{-9} Torr) deposition system following the procedure described in Ref. [32]. Briefly, the MgO(001) substrates are cut from $0.5 \times 10 \times 10$ mm^3, 99.95% pure crystals (purchased from MTI), cleaned

via sonication sequentially in acetone, isopropyl alcohol, and deionized water, and oven-baked in air at 523 K for one hour. The samples are mounted on a pyrolytic boron nitride heating stage [33], where they are held by Mo clips, transferred to the main chamber, and degassed by resistively heating to and holding at 1273 K until the chamber pressure is below 6×10^{-9} Torr. The sample temperature T_s is then set to the desired value. In our experiments, we estimate that the maximum variation in T_s across the substrate is ± 100 K. The magnetron sputter-deposition is carried out using a 3.2-mm-thick × 50.8 mm diameter Zr target (99.91 wt.% pure with 0.08 wt.% Hf from ACI Alloys, Inc.), located at about 30 cm directly above the substrate. The chamber is first filled with ethylene (99.999% purity) gas up to the desired pressure $p_{C_2H_4}$ between 2×10^{-7} Torr and 2×10^{-4} Torr set using a UHV leak valve. Subsequently, Ar (99.999% purity) gas is let in and the total pressure is adjusted to 10 mTorr. Zr-C thin films are deposited using Zr target power maintained constant at 50 W for 30 minutes. The target voltage increases with increasing $p_{C_2H_4}$ from 225 V (2×10^{-7} Torr) to 227 V (2×10^{-6} Torr and 2×10^{-5} Torr), and 234 V (2×10^{-4} Torr). Prior to deposition, the Zr target is sputter-cleaned using the same Ar/C_2H_4 composition as that used for the film growth for 2 minutes with the sample rotated out-of-sight from the target. After deposition, the ethylene and Ar gas supplies are shut off and the chamber is evacuated while the sample is passively cooled to room temperature by switching off the current supplied to the substrate heater.

XRD 2θ-ω data are obtained following the procedure described in Ref. [34] using a Jordan Valley D1 diffractometer with a sealed copper X-ray tube source, a MaxFlux specular mirror to produce a parallel beam, a two bounce channel-cut (2 2 0) Si collimator crystal to select the Cu $K_{\alpha 1}$ wavelength (λ = 0.154056 nm) for the incident beam, and a two bounce channel-cut (2 2 0) Si analyzer crystal for the third axis optics. The sample and stage are calibrated with respect to ω,

ϕ (out-of-plane rotation perpendicular to ω), and χ (in-plane rotation) about the MgO(004) peak, $2\theta = 94.0496°$. 2θ-ω scans for 2θ values between 20° and 100° are acquired using double-axis diffraction with a step size of 0.02° and a dwell time of 1 s.

Cross-sectional TEM (XTEM) samples are prepared using 30 kV Ga^+ ions in an FEI Nova 600 NanoLab DualBeam™ scanning electron microscope equipped with a focused ion beam (FIB) source. Prior to milling, the film surface is protected by ~ 150 nm and ~ 1 μm thick Pt layers deposited sequentially, first using electron beams to minimize any damage that may incur during the subsequent ion-beam-assisted deposition of the thicker layers. TEM images of the film and the film-substrate interface are acquired in an FEI Titan 80-300 kV scanning TEM (S/TEM) operated at 300 kV for imaging.

XPS data are obtained using a Kratos Analytical AXIS Ultra DLD at binding energies between 0 and 1200 eV with a pass energy of 160 eV, step size of 1.0 eV, and dwell time of 0.1 s. High-resolution Zr 3*d* and C 1*s* spectra are acquired using a pass energy of 20 eV and a step size of 0.1 eV over the energy ranges 160 – 215 eV and 264 – 300 eV, respectively, with dwell times of 0.5 s and 2 s. In order to accurately determine the bulk composition and minimize the contribution to the XPS signal from surface contamination, the XPS data are obtained after Ar^+ ion etching of all but one samples for 1 h and the other sample (grown using $p_{C_2H_4} = 2 \times 10^{-7}$ Torr and $T_s = 923$ K) for 2.5 h. The relative concentrations of Zr and C in the films are determined from the ratios of the high-resolution Zr 3*d* and C 1*s* spectral peak areas, measured using CasaXPS software and defined with a Shirley background type [35], corrected by their respective relative sensitivity factors, 2.58 and 0.278. In order to assess the accuracy of our quantification procedure, we acquired both XPS and Rutherford backscattering spectrometry (RBS) data (details below) from the same ZrC_x film (sputter-deposited on Al_2O_3(0001) using a ZrC target [36]. From

the XPS measurements, following the procedure described above, we determined the film composition as C/Zr = 1.44, while the RBS analysis yielded C/Zr = 2.04. The apparent discrepancy in the carbon contents measured using these two techniques could be due to preferential removal of C from the surface during sputter-etching of the samples prior to XPS measurements coupled with the fact that XPS is a surface-sensitive technique while RBS probes the entire cross-section of the film.

RBS-Nuclear Reaction Analysis (RBS-NRA) data, used to determine the film stoichiometry of one sample apart from the set of samples presented in this article, are obtained using 1.2 MeV deuteron beam generated by the nuclear microprobe of CEA Saclay, France. The incident deuteron beam size is $4 \times 3\ \mu m^2$. Backscattered particles produced from nuclear reactions are detected with an annular surface barrier particle detector (detection angle 170°). C concentrations are measured from the peak of the nuclear reaction $^{12}C(d,p_0)^{13}C$ and Zr concentration from that of backscattered deuterons. The film composition is deduced by fitting experimental data with simulated spectra using SIMNRA code [37], which takes into account experimental beam conditions and related cross-sections of scattering and deuteron induced nuclear reactions.

3. Results and discussion

Figure 1a shows XRD 2θ-ω scans acquired from Zr-C/MgO(001) samples (open circles) grown at T_s = 923 K using Ar/C_2H_4 gas mixtures with $p_{C_2H_4}$ between 2×10^{-7} Torr and 2×10^{-4} Torr. In Fig. 1a, the solid line is an experimental XRD 2θ-ω scan of a bare MgO(001) substrate, provided as a reference. The higher intensity peaks at 2θ = 42.9° and 41.0° labeled with asterisks (*) correspond to 002 reflections of the MgO single-crystal substrate due to Cu $K_{\alpha 1}$ (λ = 0.154056 nm) and unintentional W L_α (λ = 0.147635 nm) radiations from the X-ray source, respectively.

XRD data obtained from the layers deposited using the lowest $p_{C_2H_4}$ (= 2×10^{-7} Torr) do not show any peaks due to B1-ZrC but reveal reflections at 2θ values corresponding to hcp Zr 0002 and $10\bar{1}1$. The lattice constants (a_{Zr}, c_{Zr}) determined from the XRD data are (0.325 ± 0.003 nm, 0.517 ± 0.003 nm), which are within the measurement uncertainties the same as (0.323 nm, 0.515 nm) of pure Zr [38]. In the same XRD pattern, we also note the presence of seemingly high background intensity at 2θ ≈ 35°, highlighted by a dotted circle, between the Zr 0002 and Zr $10\bar{1}1$ peaks. We suggest and provide supporting evidence in the following section that this result is likely due to the formation of hexagonal-structured carbides, e.g., Zr_3C_2 ($P3_121$, space group 152; a_1 = 0.306 nm and c_1 = 1.491 nm), whose $10\bar{1}2$ and 0006 reflections are at 2θ = 35.9° and 36.1°, respectively. At higher $p_{C_2H_4}$ (= 2×10^{-6} Torr and 2×10^{-5} Torr), the XRD data reveal peaks corresponding to 002 and 111 reflections of B1-structured ZrC_x. We observe a shift in ZrC_x 111 reflection peak position to lower 2θ values, i.e., 111 interplanar spacing d_{111} increases, with increasing $p_{C_2H_4}$ from 2θ = 33.12° (d_{111} = 0.270 nm) at 2×10^{-6} Torr to 2θ = 32.84° (d_{111} = 0.273 nm) at 2×10^{-5} Torr. (The 002 reflections are too broad to accurately measure any variations in their peak positions and therefore we are unable to determine the existence, if any, of inhomogeneous distortions in the ZrC lattice.) From the measured d_{111} values at each $p_{C_2H_4}$, we determine a = 0.468 ± 0.004 nm at 2×10^{-6} Torr and 0.472 ± 0.004 nm at 2×10^{-5} Torr. The former is, within the measurements uncertainties, the same as a_o = 0.4693 nm of the bulk stoichiometric ZrC [1], while the latter is ~0.6 % larger than a_o, likely due to distortion of the ZrC lattice due to increased incorporation of C in the films [6,13,26,27]. Similar shifts in XRD peak positions have been previously observed with increasing carbon contents in sputter-deposited ZrC [13], HfC [26], and NbC [27] thin films. The XRD scan from the sample grown with the highest $p_{C_2H_4}$ (= 2×10^{-4} Torr) does not show any peaks, suggesting that the film is X-ray amorphous.

Based on the data in Fig. 1a, we identify $p_{C_2H_4} = 2 \times 10^{-6}$ Torr as the optimal ethylene partial pressure for the growth of B1-ZrC at $T_s = 923$ K in our deposition system.

We investigated the effect of T_s, another key parameter that can influence the crystallinity of sputter-deposited films [13,39]. Fig. 1b shows XRD data obtained from Zr-C layers sputter-deposited at 723 K ≤ T_s ≤ 1123 K using Ar/C_2H_4 gas mixtures with $p_{C_2H_4} = 2 \times 10^{-6}$ Torr. At all $T_s \leq 1023$ K, we observe two sets of peaks corresponding to B1-structured ZrC_x 111 reflection at 2θ values between 32.92° and 33.14°, and 002 reflection at around 38.52°. The lattice parameters extracted from the 002 reflection are ~0.5% smaller compared to a_o of stoichiometric ZrC [1], while those determined from the 111 reflections are ~0.3% larger (for 2θ = 32.92°) and ~0.3% smaller (for 2θ = 33.14°) than a_o. The peaks are however too broad and weak in intensity to accurately determine the temperature-dependent variations, if any, in the carbon content x, grain size, and strain. Interestingly, the XRD data obtained from the ZrC_x film grown at the highest T_s = 1123 K showed only one peak corresponding to 002 reflection, indicating that 002 texture is preferred at higher T_s. These results suggest that, in our experiments, 111 texture is promoted in sputter-deposited ZrC_x at lower T_s, a likely consequence of kinetic limitations inherent to the deposition process. Similar T_s-dependent 111 texture evolution has been reported in a variety of sputter-deposited TMC thin films [13,28,39–41].

We now present the microstructures of Zr-C layers sputter-deposited as a function of $p_{C_2H_4}$ and T_s. Figs. 2a-d are typical XTEM images obtained from the Zr-C thin films grown at T_s = 923 K using $p_{C_2H_4}$ = a) 2×10^{-7} Torr, b) 2×10^{-6} Torr, c) 2×10^{-5} Torr, and d) 2×10^{-4} Torr. We find that the film thickness increases with increasing $p_{C_2H_4}$ from 87 ± 4 nm at $p_{C_2H_4} = 2 \times 10^{-7}$ Torr to 245 ± 20 nm at $p_{C_2H_4} = 2 \times 10^{-4}$ Torr. (This is in contrast with the results reported in Ref. [13],

where the deposition rate decreases with increasing reactive gas (methane) partial pressure.) We attribute this result to the increase in the carbon content (supporting evidence provided in the following section) within the films with increasing $p_{C_2H_4}$ during sputter-deposition. The TEM images of Zr-C sample deposited using $p_{C_2H_4} = 2 \times 10^{-7}$ Torr reveal that the film is dense with smooth surface and compositionally-abrupt film-substrate interface (see Fig. 2a); these results are in striking contrast with the interfacial reactions observed during sputter-deposition of pure Zr films on Al_2O_3(0001) [33]. Lattice-resolved TEM image (for example, Fig. 2a') and corresponding Fourier transform (FT) (inset in Fig. 2a') show that the Zr-C layers deposited with the lowest $p_{C_2H_4} = 2 \times 10^{-7}$ Torr are crystalline and that the layer is primarily composed of hcp-structured Zr. We have also observed additional reflections that we attribute to trigonal-Zr_3C_2 $000\bar{3}$, the presence of which could explain the observed high background XRD intensity at $2\theta \approx 35°$ in Fig. 1a. This result suggests the coexistence of hcp-Zr and trigonal Zr_3C_2. Increasing $p_{C_2H_4}$ to 2×10^{-6} Torr and 2×10^{-5} Torr leads to porous films with dendritic columns and facetted surfaces (Figs. 2b and c). The corresponding higher resolution XTEM images in Figs. 2b' and c' reveal regions with diffraction contrast indicative of crystallinity; surrounding regions without such contrast are likely composed of amorphous C. FTs in Figs. 2b' and c' reveal reflections corresponding to B1-structured 002 and 111 grains in the films, consistent with the XRD results. FTs (not shown here) of the XTEM images acquired from the regions near the film-substrate interfaces in these two samples reveal two sets of identical reflections, indicative of cube-on-cube epitaxial growth of 002-oriented ZrC layers on the MgO(001) substrate. At the highest $p_{C_2H_4} = 2 \times 10^{-4}$ Torr used in our experiments, the layers appear to be dense (see Fig. 2d). The XTEM image in Fig. 2d' lacks any diffraction contrast and the corresponding FT shows a broad diffuse ring, commonly associated with amorphous samples. These observations suggest that the Zr-C

films deposited using 2×10^{-4} Torr ethylene are amorphous and are consistent with the XRD data (Fig. 1a).

Figs. 3a-d and 3a'-d' are series of low-magnification and higher-resolution XTEM images, respectively, obtained from near the substrate-film interfaces in the ZrC_x/MgO(001) samples grown using $p_{C_2H_4} = 2 \times 10^{-6}$ Torr at different T_s. All the TEM images reveal fully dense layers with columnar grains and corrugated surfaces, indicating that the growth morphologies and microstructures are qualitatively similar in all the samples grown at different T_s. XTEM images (not shown here) obtained along the growth direction also reveal the presence of amorphous regions throughout the films. These results are qualitatively similar to those reported in previous studies [3]. Diffraction spots corresponding to both ZrC_x 002 and 111 reflections are observed in the FTs in Figs. 3a'-c', indicating that the films are polycrystalline. The FT in Fig. 3d' shows only 002 reflections due to B1-ZrC_x, consistent with the XRD data in Fig. 1b. From the ZrC 002 reflections, we extract a values (= 0.47 ± 0.01 nm), ~ 0.5% smaller compared to a_o, and are consistent with the value determined from the XRD data. High-resolution TEM images along with their corresponding FTs (not shown here) of all samples show the presence of only 002-oriented ZrC grains at the interface with a cube-on-cube relation with respect to the MgO(001) substrate, indicative of heteroepitaxial growth during the early stages of deposition.

In order to quantify the free and the bonded carbon contents in ZrC_x in the films, we used XPS. Fig. 4a shows representative high-resolution C 1*s* and Zr 3*d* XPS data acquired from the bulk of Zr-C samples grown using different $p_{C_2H_4}$. Within these spectra, we identify peaks associated with carbon at binding energies: 284.0 ~ 284.2 eV as C-C bonds in free-carbon; 281.2 ~ 282 eV as C-Zr bonds; and 282 ~ 284 eV as C-Zr* bonds [3,5,42,43]. The XPS peak due to C-C bond in carbides is often attributed to the presence of disordered, sp^2 (graphite), and/or sp^3

240 (diamond) hybridized carbon, whose exact contributions to the XPS signal are not resolvable in
241 our measurements [6,44]. The peaks observed at binding energies between 178.1 and 180.5 eV
242 correspond to Zr $3d_{5/2}$ and Zr $3d_{3/2}$, respectively. We find that the Zr peaks are better defined at
243 lower $p_{C_2H_4}$ than at higher values, presumably due to the decrease in free-C content. With
244 increasing $p_{C_2H_4}$, we observe a shift (compared to the dashed vertical lines in the plot, which
245 correspond to binding energies in stoichiometric ZrC) in the C-Zr and Zr 3*d* peak positions to
246 higher binding energies. Based on the increase in C-C, and concomitant decrease in the C-Zr,
247 peak intensities with increasing $p_{C_2H_4}$, we suggest that the observed peak shifts are due to the
248 increase in free-C content in the films.

249 From the measurements of the Zr 3*d*, C-C, C-Zr, and C-Zr* peak areas from Fig. 4a, we
250 quantify the concentrations of total carbon, free-C, and bonded-carbon *x* in ZrC_x, plotted as
251 magenta, black, and green curves, respectively, as a function of $p_{C_2H_4}$ in Fig. 4b. The label free-C
252 in the plot refers to the elemental carbon that is not bonded to Zr and corresponds to C-C peaks in
253 Fig. 4a. We find that the amount of total C and free-C increase while the fraction of carbon
254 bonded to Zr, i.e. the carbide phase, decreases with increasing $p_{C_2H_4}$ during sputter-deposition.
255 These results are consistent with the observation of increasing fraction of amorphous phase with
256 increasing $p_{C_2H_4}$ in the TEM images in Fig. 2 and are commonly observed in sputter-deposited
257 Zr-C films [3]. Interestingly, the fraction of free-C relative to the amount of carbon in the carbide
258 phase is higher in our films than in the films deposited using three orders of magnitude higher
259 reactive gas (methane) partial pressure [3]. Possible reasons for this behavior include: differences
260 in the rates of dissociative chemisorption of carbon due to precursor composition (relatively more
261 stable methane with one C atom/molecule vs. ethylene with two C atoms/molecule), Zr
262 deposition rates, T_s, total gas pressure, plasma characteristics, and residual gas composition and

concentration. Among all these samples, based on the XPS data, we note that the films deposited using $p_{C_2H_4}$ = 2 × 10^{-6} Torr yield the highest fraction of Zr-C phase with the least amount of free-C. In the following section, we present the effect of T_s on the composition of Zr-C films deposited with $p_{C_2H_4}$ = 2 × 10^{-6} Torr.

Fig. 4c shows representative C 1*s* and Zr 3*d* spectra obtained from the Zr-C samples grown at different T_s using $p_{C_2H_4}$ = 2 × 10^{-6} Torr. From the spectra, we identify the two characteristic Zr $3d_{5/2}$ and $3d_{3/2}$ peaks. In the C 1*s* spectra, we observe one high intensity peak at ~ 281 eV, which we attribute to C-Zr bonds, and one relatively broader peak around 284 eV due to C-C bonds. With increasing T_s, we observe shifts (~ 0.3 eV) in both the Zr 3*d* and C-Zr peaks to higher binding energies, suggestive of stronger bonding presumably due to decrease in the C-content within the carbide; the magnitude of shift is more pronounced at higher T_s (≥ 923 K). In all the samples grown at different T_s, C-C peaks are broad, shallow, and changes (if any) in the peak positions are not detectable. The T_s-dependent changes in total C, free-C, and bonded-carbon concentrations are plotted in Fig. 4d. We find that the amounts of total C (magenta curve) and free-C (black curve) increase marginally with increasing T_s, indicating that substrate temperatures over 723 K have little influence on the total C and free-C contents in the Zr-C films sputter-deposited using $p_{C_2H_4}$ = 2 × 10^{-6} Torr. (These results are opposite to those reported for Zr-C films sputter-deposited using methane gas [13], which as mentioned earlier could be not only due to the use of ethylene vs. methane but also system-specific deposition parameters.) Based on these results, we suggest that during reactive sputter-deposition of Zr using low ethylene partial pressures, such as $p_{C_2H_4}$ = 2 × 10^{-6} Torr, incorporation of C from C_2H_4 into the growing films occurs readily at all $T_s \geq 723$ K.

4. Conclusions

This report presents the effects of ethylene partial pressure ($p_{C_2H_4}$) and substrate temperature (T_s) on the microstructural and compositional evolution of reactively sputter-deposited Zr-C thin films on MgO(001) substrates using ultra-high vacuum dc magnetron sputtering of Zr target in Ar/C_2H_4 gas mixtures with fairly low $p_{C_2H_4} \leq 2\%$ of the total pressure. We find that all the Zr-C films, irrespective of the $p_{C_2H_4}$ and T_s, are polycrystalline two-phase mixtures composed of hexagonal close-packed Zr:C solid solutions (at ultra-low $p_{C_2H_4} = 0.002\%$) or B1-ZrC_x (at higher $p_{C_2H_4}$) and free-C. The amount of free-C incorporated into the films depends sensitively on $p_{C_2H_4}$ at T_s = 923 K. Increasing the T_s above 723 K (with $p_{C_2H_4} = 2 \times 10^{-6}$ Torr) has little effect on the carbon incorporation rate. Our results indicate that relatively small amount of ethylene gas (0.02% of the total pressure in our experiments) is sufficient to deposit two-phase mixtures of ZrC and free-carbon. Given that pure, single-phase carbide films are often desirable, we suggest that reactive sputter-deposition of ZrC (and other TMC) films is probably best carried out using ultra-low partial pressures of carbon containing precursors; the exact pressure however depends on the deposition system, substrate temperature, deposition rate, and the precursor.

Acknowledgements

We gratefully acknowledge support from the Air Force Office of Scientific Research (AFOSR, Dr. Ali Sayir) under Grant # FA9550-14-1-0106 and # FA9550-18-1-0050. We thank the Office of Naval Research (Dr. Chagaan Baatar) for the funds received under Grant #N00014-12-1-0518 used to build the UHV deposition system. KT is supported by the Japanese Student Service Organization (L16111111026) and the UCLA department of materials science and engineering for his doctoral study in the United States. AA is supported by the National Science Foundation

(NSF CMMI) grant #1563427 (Dr. Kara Peters). We thank Mr. Noah Bodzin and the Nanoelectronics Research Facility in the UCLA Henry Samueli School of Engineering for assistance with focused ion beam milling and acknowledge the use of instruments at the Electron Imaging Center for NanoMachines supported by NIH (1S10RR23057) and the California NanoSystems Institute at UCLA.

References

[1] M. Morris, E.H. Evans, H.S. Parker, W. Wong-Ng, D.M. Gladhill, C.R. Hubbard, Standard x-ray diffraction powder patterns, National Bureau of Standards, 1984. http://archive.org/details/standardxraydiff2521morr (accessed March 18, 2019).

[2] H.O. Pierson, Handbook of Refractory Carbides and Nitrides: Properties, Characteristics, Processing and Applications, Elsevier Science, New Jersey, USA, 1996.

[3] Q.N. Meng, M. Wen, F. Mao, N. Nedfors, U. Jansson, W.T. Zheng, Deposition and characterization of reactive magnetron sputtered zirconium carbide films, Surface and Coatings Technology. 232 (2013) 876–883. https://doi.org/10.1016/j.surfcoat.2013.06.116.

[4] S. Norgren, J. García, A. Blomqvist, L. Yin, Trends in the P/M hard metal industry, International Journal of Refractory Metals and Hard Materials. 48 (2015) 31–45. https://doi.org/10.1016/j.ijrmhm.2014.07.007.

[5] M. Andersson, S. Urbonaite, E. Lewin, U. Jansson, Magnetron sputtering of Zr–Si–C thin films, Thin Solid Films. 520 (2012) 6375–6381. https://doi.org/10.1016/j.tsf.2012.06.044.

[6] L.E. Toth, Transition metal carbides and nitrides, Academic Press, 1971.

[7] J. Balko, T. Csanádi, R. Sedlák, M. Vojtko, A. KovalĽíková, K. Koval, P. Wyzga, A. Naughton-Duszová, Nanoindentation and tribology of VC, NbC and ZrC refractory carbides, Journal of the European Ceramic Society. 37 (2017) 4371–4377. https://doi.org/10.1016/j.jeurceramsoc.2017.04.064.

[8] F. Monteverde, A. Bellosi, L. Scatteia, Processing and properties of ultra-high temperature ceramics for space applications, Materials Science and Engineering: A. 485 (2008) 415–421. https://doi.org/10.1016/j.msea.2007.08.054.

[9] K. Minato, T. Ogawa, K. Fukuda, H. Nabielek, H. Sekino, Y. Nozawa, I. Takahashi, Fission product release from ZrC-coated fuel particles during postirradiation heating at 1600°C, Journal of Nuclear Materials. 224 (1995) 85–92. https://doi.org/10.1016/0022-3115(95)00032-1.

[10] S. Ueta, J. Aihara, A. Yasuda, H. Ishibashi, T. Takayama, K. Sawa, Fabrication of uniform ZrC coating layer for the coated fuel particle of the very high temperature reactor, Journal of Nuclear Materials. 376 (2008) 146–151. https://doi.org/10.1016/j.jnucmat.2008.02.068.

[11] Y. Katoh, G. Vasudevamurthy, T. Nozawa, L.L. Snead, Properties of zirconium carbide for nuclear fuel applications, Journal of Nuclear Materials. 441 (2013) 718–742. https://doi.org/10.1016/j.jnucmat.2013.05.037.

[12] W.A. Mackie, P.R. Davis, Single-crystal zirconium carbide as a high-temperature thermionic cathode material, IEEE Transactions on Electron Devices. 36 (1989) 220–224. https://doi.org/10.1109/16.21209.

[13] J. Brückner, T. Mäntylä, Reactive magnetron sputtering of zirconium carbide films using Ar-CH4 gas mixtures, Surface and Coatings Technology. 59 (1993) 166–170. https://doi.org/10.1016/0257-8972(93)90077-2.

[14] J. Xu, S. Jiang, Y. Wang, S. Shang, D. Miao, R. Guo, Photo-thermal conversion and thermal insulation properties of ZrC coated polyester fabric, Fibers Polym. 18 (2017) 1938–1944. https://doi.org/10.1007/s12221-017-1237-z.

[15] X.-H. Gao, H.-X. Guo, T.-H. Zhou, G. Liu, Optical properties and failure analysis of ZrC-ZrOx ceramic based spectrally selective solar absorbers deposited at a high substrate temperature, Solar Energy Materials and Solar Cells. 176 (2018) 93–99. https://doi.org/10.1016/j.solmat.2017.11.018.

[16] M. Balden, B.T. Cieciwa, I. Quintana, E. de Juan Pardo, F. Koch, M. Sikora, B. Dubiel, Metal-doped carbon films obtained by magnetron sputtering, Surface and Coatings Technology. 200 (2005) 413–417. https://doi.org/10.1016/j.surfcoat.2005.02.218.
[17] M. Dollé, D. Gosset, C. Bogicevic, F. Karolak, D. Simeone, G. Baldinozzi, Synthesis of nanosized zirconium carbide by a sol–gel route, Journal of the European Ceramic Society. 27 (2007) 2061–2067. https://doi.org/10.1016/j.jeurceramsoc.2006.06.005.
[18] K. Minato, T. Ogawa, T. Koya, H. Sekino, T. Tomita, Retention of fission product caesium in ZrC-coated fuel particles for high-temperature gas-cooled reactors, Journal of Nuclear Materials. 279 (2000) 181–188. https://doi.org/10.1016/S0022-3115(00)00015-5.
[19] G.H. Reynolds, Chemical vapor deposition of ZrC on pyrocarbon-coated fuel particles, J. Nucl. Mater., v. 50, No. 2, Pp. 215-216. (1974). https://doi.org/10.1016/0022-3115(74)90158-5.
[20] Y.S. Won, V.G. Varanasi, O. Kryliouk, T.J. Anderson, L. McElwee-White, R.J. Perez, Equilibrium analysis of zirconium carbide CVD growth, Journal of Crystal Growth. 307 (2007) 302–308. https://doi.org/10.1016/j.jcrysgro.2007.05.039.
[21] V. Craciun, J. Woo, D. Craciun, R.K. Singh, Epitaxial ZrC thin films grown by pulsed laser deposition, Applied Surface Science. 252 (2006) 4615–4618. https://doi.org/10.1016/j.apsusc.2005.07.139.
[22] L. D'Alessio, A. Santagata, R. Teghil, M. Zaccagnino, I. Zaccardo, V. Marotta, D. Ferro, G. De Maria, Zirconium carbide thin films deposited by pulsed laser ablation, Applied Surface Science. 168 (2000) 284–287. https://doi.org/10.1016/S0169-4332(00)00625-5.
[23] E. Portolan, C.L.G. Amorim, G.V. Soares, C. Aguzzoli, C.A. Perottoni, I.J.R. Baumvol, C.A. Figueroa, Carbon occupancy of interstitial sites in vanadium carbide films deposited by direct current reactive magnetron sputtering, Thin Solid Films. 517 (2009) 6493–6496. https://doi.org/10.1016/j.tsf.2009.03.202.
[24] X. Wu, G. Li, Y. Chen, G. Li, Microstructure and mechanical properties of vanadium carbide coatings synthesized by reactive magnetron sputtering, International Journal of Refractory Metals and Hard Materials. 27 (2009) 611–614. https://doi.org/10.1016/j.ijrmhm.2008.09.014.
[25] A.Z. Ait Djafer, N. Saoula, N. Madaoui, A. Zerizer, Deposition and characterization of titanium carbide thin films by magnetron sputtering using Ti and TiC targets, Applied Surface Science. 312 (2014) 57–62. https://doi.org/10.1016/j.apsusc.2014.05.084.
[26] G. Li, G. Li, Microstructure and mechanical properties of hafnium carbide coatings synthesized by reactive magnetron sputtering, J Coat Technol Res. 7 (2010) 403–407. https://doi.org/10.1007/s11998-009-9225-x.
[27] K. Zhang, M. Wen, G. Cheng, X. Li, Q.N. Meng, J.S. Lian, W.T. Zheng, Reactive magnetron sputtering deposition and characterization of niobium carbide films, Vacuum. 99 (2014) 233–241. https://doi.org/10.1016/j.vacuum.2013.06.012.
[28] S.S. Kumar, A. Sharma, G.M. Rao, S. Suwas, Investigations on the effect of substrate temperature on the properties of reactively sputtered zirconium carbide thin films, Journal of Alloys and Compounds. 695 (2017) 1020–1028. https://doi.org/10.1016/j.jallcom.2016.10.225.
[29] N.C. Zoita, V. Braic, M. Danila, A.M. Vlaicu, C. Logofatu, C.E.A. Grigorescu, M. Braic, Influence of film thickness on the morphological and electrical properties of epitaxial TiC films deposited by reactive magnetron sputtering on MgO substrates, Journal of Crystal Growth. 389 (2014) 92–98. https://doi.org/10.1016/j.jcrysgro.2013.11.076.

[30] D.D. Kumar, N. Kumar, S. Kalaiselvam, R. Radhika, S. Dash, A.K. Tyagi, R. Jayavel, Reactive magnetron sputtered wear resistant multilayer transition metal carbide coatings: microstructure and tribo-mechanical properties, RSC Adv. 5 (2015) 81790–81801. https://doi.org/10.1039/C5RA16465F.
[31] K. Tanaka, A. Aleman, M.E. Liao, Y. Wang, M.S. Goorsky, S. Kodambaka, Effects of ultra-low ethylene partial pressure on microstructure and composition of reactively sputter-deposited Ta–C thin films, Thin Solid Films. 688 (2019) 137440. https://doi.org/10.1016/j.tsf.2019.137440.
[32] J. Fankhauser, M. Sato, D. Yu, A. Ebnonnasir, M. Kobashi, M.S. Goorsky, S. Kodambaka, Growth and characterization of epitaxial Zr(0001) thin films on Al2O3(0001), Journal of Vacuum Science & Technology A. 34 (2016) 050606. https://doi.org/10.1116/1.4961452.
[33] K. Tanaka, J. Fankhauser, H. Zaid, A. Aleman, M. Sato, D. Yu, A. Ebnonnasir, C. Li, M. Kobashi, M.S. Goorsky, S. Kodambaka, Kinetics of Zr-Al intermetallic compound formation during ultra-high vacuum magnetron sputter-deposition of Zr/Al2O3(0001) thin films, Acta Materialia. 152 (2018) 34–40. https://doi.org/10.1016/j.actamat.2018.04.018.
[34] A. Aleman, C. Li, H. Zaid, H. Kindlund, J. Fankhauser, S.V. Prikhodko, M.S. Goorsky, S. Kodambaka, Ultrahigh vacuum dc magnetron sputter-deposition of epitaxial Pd(111)/Al2O3(0001) thin films, Journal of Vacuum Science & Technology A. 36 (2018) 030602. https://doi.org/10.1116/1.5021609.
[35] N. Fairley, A. Carrick, Casa XPS User's Manual, (2001).
[36] J.P. Fankhauser, Growth and Characterization of Zr and ZrC Thin Films on Al2O3(0001), UCLA, 2016. https://escholarship.org/uc/item/6db4489v (accessed February 15, 2020).
[37] M. Mayer, SIMNRA, a simulation program for the analysis of NRA, RBS and ERDA, AIP Conference Proceedings. 475 (1999) 541–544. https://doi.org/10.1063/1.59188.
[38] A.I. Kolesnikov, A.M. Balagurov, I.O. Bashkin, A.V. Belushkin, E.G. Ponyatovsky, M. Prager, Neutron scattering studies of ordered gamma -ZrD, J. Phys.: Condens. Matter. 6 (1994) 8977–8988. https://doi.org/10.1088/0953-8984/6/43/004.
[39] C. Aguzzoli, C.A. Figueroa, G.V. Soares, I.J.R. Baumvol, Physicochemical and structural characteristics of TiC and VC thin films deposited by DC reactive magnetron sputtering, J Mater Sci. 45 (2010) 4994–5001. https://doi.org/10.1007/s10853-010-4364-0.
[40] H. Colder, R. Rizk, M. Morales, P. Marie, J. Vicens, I. Vickridge, Influence of substrate temperature on growth of nanocrystalline silicon carbide by reactive magnetron sputtering, Journal of Applied Physics. 98 (2005) 024313. https://doi.org/10.1063/1.1985975.
[41] C.-S. Chen, C.-P. Liu, C.-Y.A. Tsao, Influence of growth temperature on microstructure and mechanical properties of nanocrystalline zirconium carbide films, Thin Solid Films. 479 (2005) 130–136. https://doi.org/10.1016/j.tsf.2004.11.196.
[42] A. Escudeiro, N.M. Figueiredo, T. Polcar, A. Cavaleiro, Structural and mechanical properties of nanocrystalline Zr co-sputtered a-C(:H) amorphous films, Applied Surface Science. 325 (2015) 64–72. https://doi.org/10.1016/j.apsusc.2014.11.015.
[43] U. Jansson, E. Lewin, Sputter deposition of transition-metal carbide films — A critical review from a chemical perspective, Thin Solid Films. 536 (2013) 1–24. https://doi.org/10.1016/j.tsf.2013.02.019.
[44] R. Blume, D. Rosenthal, J.-P. Tessonnier, H. Li, A. Knop-Gericke, R. Schlögl, Characterizing Graphitic Carbon with X-ray Photoelectron Spectroscopy: A Step-by-Step Approach, ChemCatChem. 7 (2015) 2871–2881. https://doi.org/10.1002/cctc.201500344.

List of Figures

Fig. 1. 2θ-ω X-ray diffraction (XRD) data obtained from Zr-C/MgO(001) samples sputter-deposited in 10 mTorr Ar/C_2H_4 gas mixtures at (a) T_s = 923 K with 2×10^{-7} Torr ≤ $p_{C_2H_4}$ ≤ 2×10^{-4} Torr and (b) 723 K ≤ T_s ≤ 1123 K using $p_{C_2H_4} = 2 \times 10^{-6}$ Torr. An XRD scan of MgO(001) substrate (solid line) is plotted as a reference. The peaks labeled with * denote MgO 002 reflections due to Cu Kα at 2θ = 42.9° and W Lα at 2θ = 40.94°. The vertical dashed lines identify the 111 and 002 reflections in stoichiometric B1-ZrC and 0002 and $10\bar{1}1$ reflections in hcp-Zr. The dotted circle highlights the high background intensity at 2θ ~ 35°.

Fig. 2. Typical bright-field cross-sectional transmission electron microscopy (XTEM) images of Zr-C/MgO(001) samples grown at T_s = 923 K with $p_{C_2H_4}$ = (a) 2×10^{-7} Torr, (b) 2×10^{-6} Torr, (c) 2×10^{-5} Torr, and (d) 2×10^{-4} Torr. (a'-d') Higher resolution XTEM images of the samples in (a-d), respectively. The insets are the Fourier transforms (FTs) of the images in a'-d'. Cyan, purple, red, and green circles highlight Zr 0002, Zr_3C_2 $000\bar{3}$, ZrC 002, and ZrC 111 reflections, respectively. The absence of any spots in the Fig. 2d' FT implies that the region within the field of view is likely amorphous.

Fig. 3. Bright-field XTEM images of Zr-C/MgO(001) samples sputter-deposited using $p_{C_2H_4} = 2 \times 10^{-6}$ Torr at T_s = (a) 723 K, (b) 823 K, (c) 1023 K, and (d) 1123 K. All the samples appear dense with columnar microstructures and smoother surfaces. (a'-d') Representative higher-resolution XTEM images with corresponding FTs as insets of the samples in (a-d), respectively.

All the TEM images show crystalline and amorphous regions. ZrC 002 and 111 reflections are highlighted using red and green circles in the FTs, respectively.

Fig. 4. (a) X-ray photoelectron spectroscopy (XPS) data acquired around Zr 3*d* (175 – 190 eV) and C 1*s* (279 – 288 eV) from sputter-etched Zr-C samples deposited as a function of $p_{C_2H_4}$. (b) Total, free, and bonded carbon concentrations extracted from the XPS data plotted as a function of $p_{C_2H_4}$. (c) XPS data of sputter-etched Zr-C samples deposited as a function of T_s. (d) Plot of total, free, and bonded carbon concentrations *vs.* T_s. In both (a) and (c), the dashed vertical lines correspond to binding energies in stoichiometric ZrC; black, purple, and light magenta curves correspond to C-C, C-Zr, and C-Zr* components, respectively. In the plots (b) and (d), magenta, black, and green curves represent the total C, free-C, and bonded carbon (labeled 'C in Zr-C') contents in the Zr-C samples, respectively.

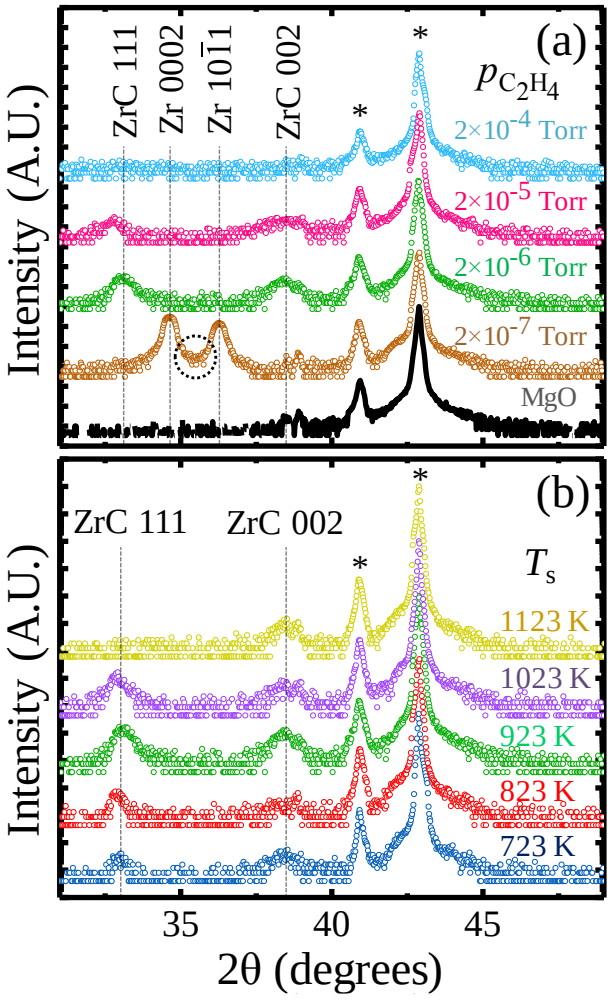

(a)
ZrC 111
Zr 0002
Zr 10$\bar{1}$1
ZrC 002
*
*
$p_{C_2H_4}$
2×10^{-4} Torr
2×10^{-5} Torr
2×10^{-6} Torr
2×10^{-7} Torr
MgO
Intensity (A.U.)
(b)
ZrC 111
ZrC 002
*
*
T_s
1123 K
1023 K
923 K
823 K
723 K
Intensity (A.U.)
35
40
45
2θ (degrees)

Figure 1

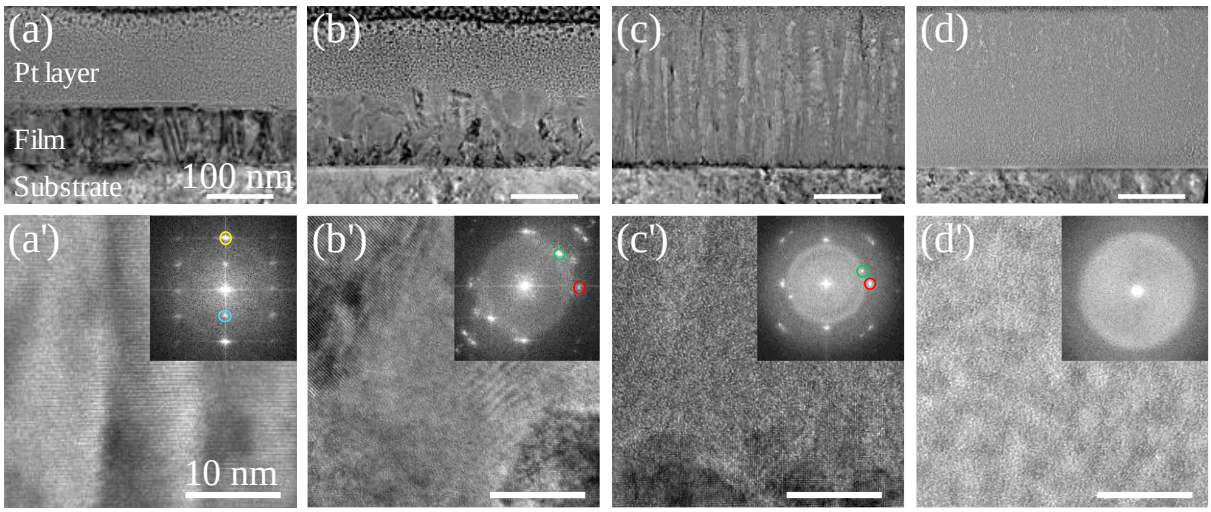


Figure 2

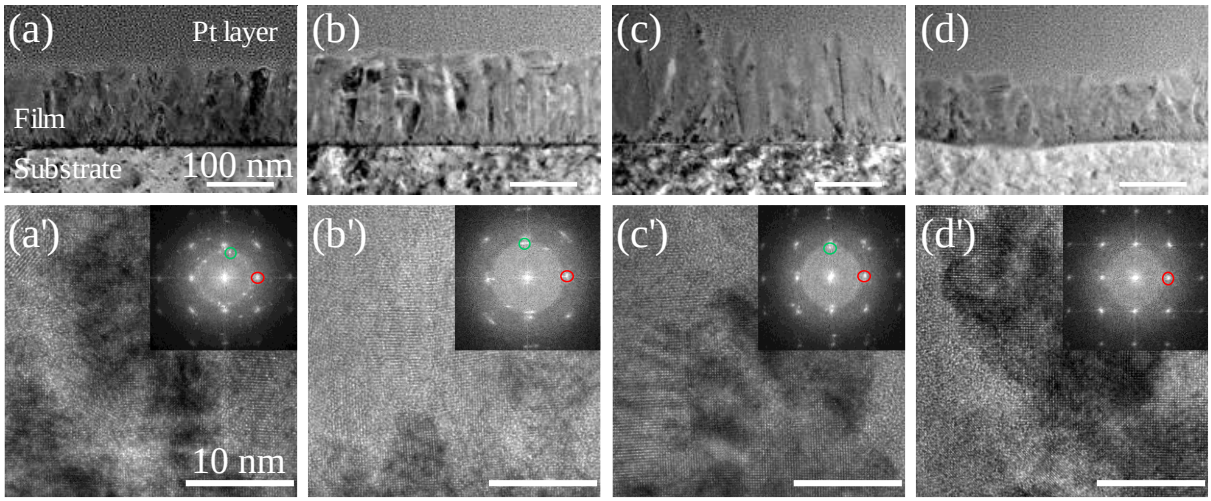


Figure 3

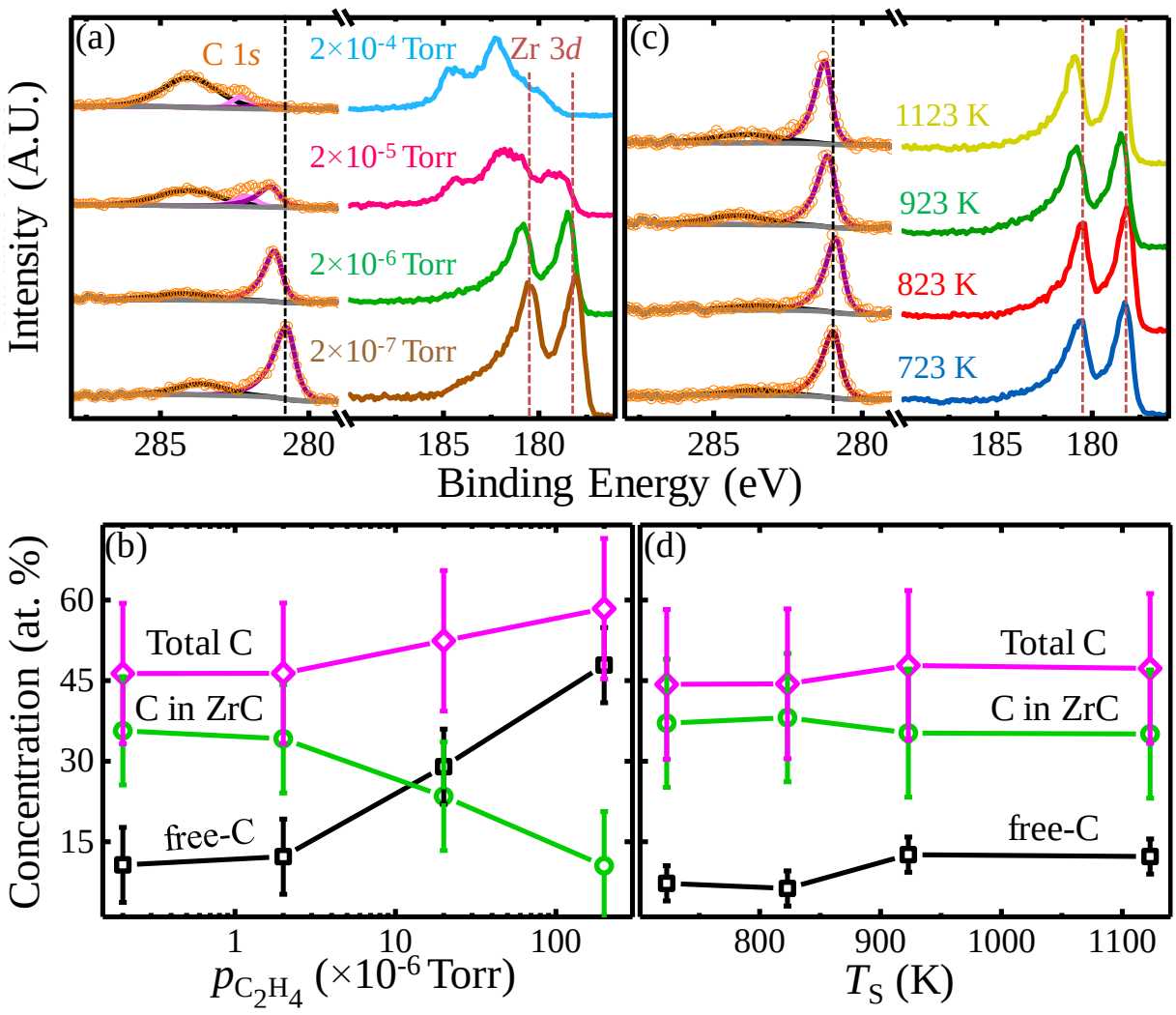

(a)
C 1s
2×10-4 Torr
Zr 3d
2×10-5 Torr
2×10-6 Torr
2×10-7 Torr
Intensity (A.U.)
285
280
185
180
(c)
1123 K
923 K
823 K
723 K
285
280
185
180
Binding Energy (eV)
(b)
Total C
C in ZrC
free-C
Concentration (at. %)
60
45
30
15
1
10
100
pC2H4 (×10-6 Torr)
(d)
Total C
C in ZrC
free-C
800
900
1000
1100
TS (K)

Figure 4